INSTITUTE OF PHYSICS PUBLISHING JOURNAL OF PHYSICS: CONDENSED MATTER

J. Phys.: Condens. Matter **13** (2001) 8587–8606 PII: S0953-8984(01)24868-1

Ab initio angle-resolved photoemission in multiple-scattering formulation

M Lüders[1], A Ernst[1,2], W M Temmerman[1], Z Szotek[1] and P J Durham[1]

[1] Daresbury Laboratory, Daresbury, Warrington WA4 4AD, Cheshire, UK
[2] Max Planck Institut für Mikrostrukturphysik, Halle, Germany

Received 16 May 2001
Published 7 September 2001
Online at stacks.iop.org/JPhysCM/13/8587

Abstract

The theory of *ab initio* semi-relativistic angle-resolved photoemission calculations is formulated within the real-space multiple-scattering theory and the single-particle approximation. It has the flexibility and simplicity required for studying systems with layered structures and more general complex geometries. For layered structures the layer-resolved potentials are obtained self-consistently using the Korringa–Kohn–Rostoker (KKR) method. The advantage of the present approach is that the self-consistent potential and the photocurrent are treated on the same footing and calculated within the same formalism. The approach is illustrated through a study of the angle-resolved photoemission for real-space, layered systems with two-dimensional periodicity, with specific application to Cu.

1. Introduction

Angle-resolved photoemission spectroscopy (ARPES) experiments are among the most powerful tools for studying the electronic structure of solids, and recent improvements in their technical realization and flexibility have led to new challenging applications, such as in the study of the superconducting gap in high-T_c materials [1, 2]. In particular, a lot of progress has been made in the study of magnetic transition metals and their compounds [3, 4], rare earths [5, 6], actinides, semiconductors, and high-temperature superconductors [1, 2]. Photoemission spectroscopy has been successfully applied to study both ordered and disordered solids and their surfaces, thin films, multilayers, and even monatomic wires [4]. However, the interpretation of measured spectra is a complex task, since they contain information on both the initial and final states of the emitted electron. Therefore, ARPES only reaches its full potential when combined with theoretical interpretations of the experiments, which can then provide information about the states involved, and how they contribute to the observed spectra.

Most state-of-the-art electronic structure calculations are based on density functional theory (DFT) [7–9]. Although it is a well known fact that the resulting Kohn–Sham (KS) energies and orbitals do not describe real excitations of the many-body system, they often

provide surprisingly good approximations to them. But even in strongly correlated systems, where this is not the case, and both the width and the positions of the bands are not well reproduced, the photocurrent, calculated from these KS states, might help experimentalists to identify measured structures, using the symmetries of the bands and their global features. For a proper and quantitative treatment of photoemission, especially in strongly correlated systems, one would, of course, have to perform calculations based on the full one-particle Green's function, such as that calculated within the *GW* approximation [10], rather than the KS Green's functions. This, however, is not the purpose of this communication. Here we want to propose and demonstrate a fast and flexible method for calculating the photocurrent, which should allow for quick calculations even for larger systems, and should help experimentalists, when it is used in combination with electronic structure calculation and the calculation of spectral functions, to identify the observed bands.

Many theories of ARPES [11, 12] have been implemented and give good results, but most of them are too complicated and restricted to special symmetries of the system. In this paper we describe an *ab initio* computational approach to ARPES, based on multiple-scattering theory within the independent-particle approximation. The main advantage of the present approach is a unified treatment of the electronic structure and the photocurrent, using the Green's function method developed by Györffy and Stott [13]. Following the concept of the real-space photoemission formalism, the Green's functions in the photocurrent formula can be expressed through the scattering matrix, τ, in the real-space representation. The real-space multiple-scattering theory offers a fertile field for investigations of systems with arbitrary arrangement of atoms. By making the appropriate Fourier transformation, the formalism can easily be specialized to more symmetric systems, such as surfaces or multilayers.

In the present approach the self-consistent potentials for the photocurrent calculations have been obtained using the same formalism as for the photocurrent. We have implemented the KKR method [14, 15] in both the traditional (unscreened) and the screened representations of the method [16–21].

The remainder of the paper is organized as follows. In section 2 the formalism is outlined and the multiple-scattering representation of the photocurrent is derived. In section 3 we show the spectra (for normal emission and off-normal emission) for the low-index surfaces of Cu and show how the spectra can be interpreted using the spectral functions of the system. Finally, in section 4 some calculations are presented that enable us to discuss the size convergence of the method and to point out further approximations, which can be used to speed up the calculations. Also the role of the self-energies in the spectra is discussed.

2. Formalism

In this section we briefly summarize the formalism of the angle-resolved photoemission within the independent-particle approximation and derive the expression for the photocurrent in the τ-matrix representation [22, 23]. A preliminary account of this formalism has been given in reference [24].

In the photoemission process an electron absorbs a photon with the energy $\hbar\omega$ and is excited into a formally unoccupied state. If its energy is high enough to overcome the surface barrier, the electron can escape into the vacuum and eventually reach the detector. On its way through the solid the electron undergoes scattering processes with the lattice, the other electrons, and the phonons. The former will be treated by the multiple-scattering theory, while the latter processes are many-particle processes, which are accounted for by the self-energy. The whole process can be described by non-equilibrium many-particle perturbation theory, as presented by Caroli *et al* [25]. Here we will use the lowest order only, in which the photocurrent

at distance R is given by

$$R^2 J^\lambda(\epsilon,\omega) = \frac{k}{4\pi}\frac{1}{(c\pi)^2}\int \mathrm{d}^3 r \int \mathrm{d}^3 r'\ \Psi_>(\boldsymbol{r};\boldsymbol{k})\hat{O}^\lambda(\boldsymbol{r})\,\Im G^r(\boldsymbol{r},\boldsymbol{r}';\epsilon) \times \hat{O}^{\lambda\dagger}(\boldsymbol{r}')\Psi^*_>(\boldsymbol{r}';\boldsymbol{k})\Theta(E_F-\epsilon)\Theta(\epsilon+\omega-V_{\mathrm{vac}}) \tag{1}$$

where $G^r(\boldsymbol{r},\boldsymbol{r}';\epsilon)$ is the retarded KS Green's function of the system, E_F is the Fermi energy, and V_{vac} is the vacuum potential;

$$\hat{O}^\lambda(\boldsymbol{r}) = \frac{1}{2c}\left[\boldsymbol{A}^\lambda(\boldsymbol{r})\hat{\boldsymbol{p}} - \hat{\boldsymbol{p}}\boldsymbol{A}^\lambda(\boldsymbol{r})\right] \tag{2}$$

describes the interaction with λ-polarized light, and $\Psi_>(\boldsymbol{r};\boldsymbol{k})$ is the so-called time-reversed LEED state, representing electrons leaving the solid into the vacuum. It is derived from the asymptotic form of the Green's function and can be expressed via

$$\Psi_>(\boldsymbol{r},\boldsymbol{k}) = \mathrm{e}^{\mathrm{i}\boldsymbol{k}\cdot\boldsymbol{r}} + \int \mathrm{d}^3 r'\ \mathrm{e}^{\mathrm{i}\boldsymbol{k}\cdot\boldsymbol{r}'} v(\boldsymbol{r}')G^r(\boldsymbol{r}',\boldsymbol{r};\tilde{\epsilon}) \tag{3}$$

where $\tilde{\epsilon} = \epsilon + \omega$ and $\boldsymbol{k}$ is defined by

$$\begin{aligned} k_x &= -\sqrt{\tilde{\epsilon}}\sin\theta_k\cos\phi_k \\ k_y &= -\sqrt{\tilde{\epsilon}}\sin\theta_k\sin\phi_k \\ k_z &= -\sqrt{\tilde{\epsilon}}\cos\theta_k. \end{aligned} \tag{4}$$

θ_k and ϕ_k are the azimuthal and polar emission angles. In this section all energies are measured with respect to the vacuum level.

Now our aim is to express all quantities involved in the photocurrent in terms of the multiple-scattering theory [14, 15]. For simplicity we use the atomic sphere approximation (ASA) in which the atomic spheres are slightly overlapping and space filling. The retarded KS Green's function of the system in the scattering-matrix representation reads as follows:

$$G^r(\boldsymbol{r},\boldsymbol{r}';\epsilon) = \sum_{LL'} \bar{Z}^i_L(\boldsymbol{r}_i;\epsilon)\tau^{ij}_{LL'}(\epsilon)Z^j_{L'}(\boldsymbol{r}'_j;\epsilon) - \sum_L \bar{Z}^i(\boldsymbol{r}_<;\epsilon)J^i_L(\boldsymbol{r}_>;\epsilon)\delta_{ij}. \tag{5}$$

The coordinates $\boldsymbol{r}_i = \boldsymbol{r} - \boldsymbol{R}_i$ are relative to the site i. $Z^i_L(\boldsymbol{r}_i;\epsilon)$ and $J^i_L(\boldsymbol{r}_i;\epsilon)$ are respectively the regular and irregular solutions of the Schrödinger equation with the single-site muffin-tin potential $v(\boldsymbol{r})$ at the energy ϵ. They can be decomposed into radial functions and spherical harmonics:

$$Z^i_L(\boldsymbol{r}_i;\epsilon) = Z^i_l(r_i;\epsilon)Y_L(\Omega) \tag{6}$$

$$J^i_L(\boldsymbol{r}_i;\epsilon) = J^i_l(r_i;\epsilon)Y_L(\Omega). \tag{7}$$

We use the shorthand notation L for the angular momentum quantum numbers l and m and define $\bar{Z}^i_L(\boldsymbol{r}_i;\epsilon)$ as

$$\bar{Z}^i_L(\boldsymbol{r}_i;\epsilon) = Z^i_l(r_i;\epsilon)Y^*_L(\Omega). \tag{8}$$

The scattering path operator $\tau^{ij}_{L_1L_2}(\varepsilon)$, which is the central quantity in multiple-scattering theory, is obtained from the matrix equation

$$[\underline{\tau}(\varepsilon)] = \left[\underline{t}^{-1}(\varepsilon) - \underline{g}(\varepsilon)\right]^{-1} \tag{9}$$

where $\underline{t}(\varepsilon)$ is the single-site scattering matrix:

$$t^i_l(\varepsilon) = \kappa^{-1}\sin(\delta^i_l(\varepsilon))\exp(\mathrm{i}\delta^i_l(\varepsilon)) \tag{10}$$

describing the scattering off a single potential. The phase shifts $\delta^i_l(\varepsilon)$ are obtained by matching the single-site wave functions Z and J at the atomic sphere radius to the solutions of the constant

muffin-tin-zero potential v_{MTZ} in the interstitial space. κ is defined as $\kappa = \sqrt{\epsilon - v_{\mathrm{MTZ}}}$. The real-space structure constants $\underline{g}(\varepsilon)$, which describe the propagation between the atomic sites, are defined by

$$g^{ij}_{LL'} = -4\pi\sqrt{\varepsilon}(-1)^m \mathrm{i}^{(l'-l)} \sum_{L''} \mathrm{i}^{-l''} C(-L, L', L'') h^+_{l''}(\boldsymbol{R}_i - \boldsymbol{R}_j). \tag{11}$$

Here $C(-L, L', L'')$ are the Gaunt coefficients, and $h^+_l(\boldsymbol{r})$ are the Hankel functions. Further details can be found in the literature on the multiple-scattering method, e.g. reference [26]. Alternatively the scattering matrix can be obtained using the screened KKR method [17, 18].

The LEED state can also be written in terms of the scattering matrix and the radial wave functions:

$$\Psi_>(\boldsymbol{r}; \boldsymbol{k}) = 4\pi \sum_j \mathrm{e}^{\mathrm{i}\boldsymbol{k}\cdot\boldsymbol{R}_j} \sum_{LL'} \mathrm{i}^l Y^*_L(\hat{\boldsymbol{k}}) \tau^{ji}_{LL'}(\tilde{\epsilon}) Z^i_{L'}(\boldsymbol{r}_i; \tilde{\epsilon}). \tag{12}$$

It remains to cast the perturbation operator $\hat{O}^\lambda(\boldsymbol{r})$ into the appropriate form. In the spirit of the single-particle approximation we neglect effects due to the dielectric function of the material, and do not calculate the vector potential self-consistently. In the Coulomb gauge ($\boldsymbol{\nabla} \cdot \boldsymbol{A}(\boldsymbol{r}) = 0$) the perturbation operator, as it appears in the matrix elements, is equivalent to

$$\hat{O}^\lambda(\boldsymbol{r}) = \frac{\mathrm{i}}{\omega} \boldsymbol{A}(\boldsymbol{r}) \cdot \big(\boldsymbol{\nabla} v(\boldsymbol{r})\big) \tag{13}$$

where the gradient operator acts *only* on the potential [12]. In this gauge the vector potential is given by

$$\boldsymbol{A}^\lambda(\boldsymbol{r}) = \boldsymbol{A}^\lambda \mathrm{e}^{\mathrm{i}\boldsymbol{q}\cdot\boldsymbol{r}} \tag{14}$$

and the polarization vector is

$$\begin{aligned} A^\lambda_x &= -\cos(\theta_{ph})\cos(\phi_{ph})\sin(\delta^\lambda) - \sin(\theta_{ph})\cos(\delta^\lambda) \\ A^\lambda_y &= -\cos(\theta_{ph})\sin(\phi_{ph})\sin(\delta^\lambda) + \cos(\theta_{ph})\cos(\delta^\lambda) \\ A^\lambda_z &= \sin(\theta_{ph})\sin(\delta^\lambda). \end{aligned} \tag{15}$$

The photon wave vector is

$$\begin{aligned} q_x &= \frac{\omega}{c}\sin\theta_{ph}\cos\phi_{ph} \\ q_y &= \frac{\omega}{c}\sin\theta_{ph}\sin\phi_{ph} \\ q_z &= \frac{\omega}{c}\cos\theta_{ph} \end{aligned} \tag{16}$$

where θ_{ph} and ϕ_{ph} are the angles of the photon incidence. Within the ASA, the perturbation can be decomposed into the contributions from each atomic sphere:

$$\hat{O}^\lambda(\boldsymbol{r}) = \frac{\mathrm{i}}{\omega} \sum_i \mathrm{e}^{\mathrm{i}\boldsymbol{q}\cdot\boldsymbol{R}_i} \chi^\lambda_i(\boldsymbol{r}_i) \tag{17}$$

with

$$\chi^\lambda_i(\boldsymbol{r}_i) = \boldsymbol{A}^\lambda \mathrm{e}^{\mathrm{i}\boldsymbol{q}\cdot\boldsymbol{r}_i} \cdot \big(\boldsymbol{\nabla} v(\boldsymbol{r}_i)\big). \tag{18}$$

This can be written as

$$\begin{aligned} \chi^\lambda_i(\boldsymbol{r}_i) &= 4\pi \sum_L \mathrm{i}^l j_l(qr_i) Y_L(\hat{\boldsymbol{q}}) Y^*_L(\hat{\boldsymbol{r}}_i) \big(\boldsymbol{A}^\lambda \cdot \hat{\boldsymbol{r}}_i\big) \big(\partial_r v(r_i)\big) \\ &= \frac{(4\pi)^2}{3} A^\lambda \sum_L \mathrm{i}^l j_l(qr_i) Y_L(\hat{\boldsymbol{q}}) Y^*_L(\hat{\boldsymbol{r}}_i) \left(\sum_m Y_{1,m}(\hat{\boldsymbol{A}}^\lambda) Y^*_{1,m}(\hat{\boldsymbol{r}}_i) \right) \big(\partial_r v(r)\big). \end{aligned} \tag{19}$$

Since the wavelength of the light in the range from the UV up to soft x-rays is large compared to the atomic sphere radii, the Bessel function $j_l(qr)$ will be negligible for $l > 0$ and $j_0(qr) \approx 1$. Hence we get

$$\chi_i^\lambda(\boldsymbol{r}_i) = \frac{(4\pi)^2}{3} A^\lambda \left(\sum_m Y_{1,m}(\hat{\boldsymbol{A}}^\lambda) Y_{1,m}^*(\hat{\boldsymbol{r}}_i) \right) \big(\partial_r v(r_i) \big). \tag{20}$$

We can now insert the KKR form of the Green's function (5), the LEED state (12), and the perturbation (20) into the expression for the photocurrent (1), and obtain its scattering-matrix representation. This can be decomposed into two contributions, stemming from the on-site and off-site terms in the scattering-matrix representation of the Green's function:

$$R^2 J^\lambda(\epsilon, \omega) = M^\lambda(\epsilon, \omega) + I^\lambda(\epsilon, \omega). \tag{21}$$

The off- and on-site contributions are respectively

$$\begin{aligned} M^\lambda(\epsilon, \omega) = {} & \frac{4\pi k}{(c\pi)^2 \omega^2} \Im \sum_{ij} \sum_{LL'} \sum_{L_2 L_2'} U_{L_2}^i(\boldsymbol{k}, \tilde{\epsilon}) \\ & \times F_{L_2 L}^{i\lambda(1)}(\epsilon, \omega) \mathrm{e}^{\mathrm{i}\boldsymbol{q}\cdot\boldsymbol{R}_i} \tau_{LL'}^{ij}(\epsilon) \mathrm{e}^{-\mathrm{i}\boldsymbol{q}\cdot\boldsymbol{R}_j} F_{L_2' L'}^{j\lambda(2)}(\epsilon, \omega) U_{L_2'}^{j*}(\boldsymbol{k}; \tilde{\epsilon}) \end{aligned} \tag{22}$$

$$I^\lambda(\epsilon, \omega) = \frac{4\pi k}{(c\pi)^2 \omega^2} \Im \sum_i \sum_{L_2 L_2'} U_{L_2}^i(\boldsymbol{k}, \tilde{\epsilon}) D_{L_2 L_2'}^{i\lambda}(\epsilon, \omega) U_{L_2'}^{i*}(\boldsymbol{k}; \tilde{\epsilon}) \tag{23}$$

where we have introduced the definitions

$$U_{L_2}^i(\boldsymbol{k}; \tilde{\epsilon}) = \sum_{L_1} \mathrm{i}^{l_1} Y_{L_1}^*(\hat{\boldsymbol{k}}) \sum_{i'} \mathrm{e}^{\mathrm{i}\boldsymbol{k}\cdot\boldsymbol{R}_{i'}} \tau_{L_1 L_2}^{i' i}(\tilde{\epsilon}) \tag{24}$$

$$F_{LL'}^{i\lambda(1)}(\epsilon, \omega) = \int \mathrm{d}^3 r_i \; Z_L^i(\boldsymbol{r}_i, \tilde{\epsilon}) \tilde{\chi}_i^\lambda(\boldsymbol{r}_i) \bar{Z}_{L'}^i(\boldsymbol{r}_i; \epsilon) \tag{25}$$

$$F_{LL'}^{i\lambda(2)}(\epsilon, \omega) = \int \mathrm{d}^3 r_i \; Z_L^{i*}(\boldsymbol{r}_i, \tilde{\epsilon}) \tilde{\chi}_i^\lambda(\boldsymbol{r}_i) Z_{L'}^i(\boldsymbol{r}_i; \epsilon) \tag{26}$$

$$D_{L_2 L_2'}^{i\lambda}(\epsilon, \omega) = \sum_L \int \mathrm{d}^3 r_i \int \mathrm{d}^3 r_i' \; Z_{L_2}^i(\boldsymbol{r}_i; \tilde{\epsilon}) \tilde{\chi}_i^\lambda(\boldsymbol{r}_i) \bar{Z}_L^i(\boldsymbol{r}_<; \epsilon) J_L^i(\boldsymbol{r}_>; \epsilon) \tilde{\chi}_i^\lambda(\boldsymbol{r}_i') Z_{L_2'}^{i*}(\boldsymbol{r}_i'; \tilde{\epsilon}). \tag{27}$$

The angular momentum integrations can be performed, leaving us with

$$\begin{aligned} F_{LL'}^{i\lambda(1)}(\epsilon, \omega) &= \frac{4\pi}{3} A^\lambda C(l, m; 1, m' - m; l', -m') (-1)^m Y_{1,m-m'}(\hat{\boldsymbol{A}}^\lambda) f_{ll'}^{i(1)}(\epsilon, \omega) \\ F_{LL'}^{i\lambda(2)}(\epsilon, \omega) &= \frac{4\pi}{3} A^\lambda C(l, m; 1, m' - m; l', -m') (-1)^m Y_{1,m-m'}^*(\hat{\boldsymbol{A}}^\lambda) f_{ll'}^{i(2)}(\epsilon, \omega) \end{aligned} \tag{28}$$

$$\begin{aligned} D_{L_2 L_2'}^{i\lambda}(\epsilon, \omega) = {} & \left(\frac{4\pi}{3} A^\lambda \right)^2 \sum_L Y_{1m+m_2}(\hat{\boldsymbol{A}}^\lambda) Y_{1,m+m_2'}^*(\hat{\boldsymbol{A}}^\lambda) \\ & \times C(l, m; 1, -(m + m_2); l_2, m_2) (-1)^{m_2} C(l, m; 1, -(m + m_2'); l_2', m_2') (-1)^{m_2'} \\ & \times \int_0^{R_i} \mathrm{d}r \; r^2 Z_{l_2}^i(r, \tilde{\epsilon}) \big(\partial_r v(r) \big) \big[J_l^i(r, \epsilon) d_{ll_2'}^{i(1)}(r, \epsilon, \omega) + Z_l^i(r, \epsilon) d_{ll_2'}^{i(2)}(r, \epsilon, \omega) \big] \end{aligned} \tag{29}$$

where the $C(l, m; l_1, m_1; l_2, m_2)$ are the Gaunt coefficients, defined by

$$C(l, m; l_1, m_1; l_2, m_2) = \int \mathrm{d}\Omega \; Y_{l,m}(\Omega) Y_{l_1,m_1}(\Omega) Y_{l_2,m_2}(\Omega). \tag{30}$$

The remaining matrix elements of the radial perturbation potential and the radial functions are simply

$$f_{ll'}^{i(1)}(\epsilon,\omega) = \int_0^{R_i} \mathrm{d}r\ r^2 Z_l^i(r;\tilde{\epsilon})\big(\partial_r v(r)\big) Z_{l'}^i(r,\epsilon) \tag{31}$$

$$f_{ll'}^{i(2)}(\epsilon,\omega) = \int_0^{R_i} \mathrm{d}r\ r^2 Z_l^{i*}(r;\tilde{\epsilon})\big(\partial_r v(r)\big) Z_{l'}^i(r,\epsilon) \tag{32}$$

$$d_{ll'}^{i(1)}(r,\epsilon,\omega) = \int_0^{r} \mathrm{d}r'\ r'^2 Z_l^i(r',\epsilon)\big(\partial_r v(r')\big) Z_{l'}^{i*}(r',\tilde{\epsilon}) \tag{33}$$

$$d_{ll'}^{i(2)}(r,\epsilon,\omega) = \int_r^{R_i} \mathrm{d}r'\ r'^2 J_l^i(r',\epsilon)\big(\partial_r v(r')\big) Z_{l'}^{i*}(r',\tilde{\epsilon}). \tag{34}$$

For systems with a two-dimensional (2D) lattice symmetry, such as surfaces or multilayers, it is advantageous to incorporate this symmetry into the formalism and perform the 2D Fourier transformations. This allows a quasi-exact treatment of the in-plane scattering process. The lattice-site vectors $\boldsymbol{R}_i$ can be decomposed as follows:

$$\boldsymbol{R}_i = \boldsymbol{R}_\parallel + \boldsymbol{S}^{u\alpha} \tag{35}$$

with u referring to the atomic position within a plane, and α labelling different planes. Employing the 2D Fourier transformed τ-matrix:

$$\tau_{L,L'}^{u\alpha,v\beta}(\boldsymbol{k}_\parallel;\epsilon) = \sum_{\boldsymbol{R}_\parallel} \mathrm{e}^{\mathrm{i}\boldsymbol{k}_\parallel \boldsymbol{R}_\parallel} \tau_{L,L'}(\boldsymbol{R}_\parallel; \boldsymbol{S}^{u\alpha}, \boldsymbol{S}^{v\beta};\epsilon) \tag{36}$$

the three-dimensional sum over the sites can be reformulated as

$$\sum_i \mathrm{e}^{\mathrm{i}\boldsymbol{k}\boldsymbol{R}_i} \tau_{L,L'}^{ij}(\epsilon) = \mathrm{e}^{\mathrm{i}\boldsymbol{k}\cdot\boldsymbol{R}'_\parallel} \sum_{u\alpha} \mathrm{e}^{\mathrm{i}\boldsymbol{k}\cdot\boldsymbol{S}^{u\alpha}} \tau_{L,L'}^{u\alpha,v\beta}(\boldsymbol{k}_\parallel;\epsilon). \tag{37}$$

This can be used to rewrite the two contributions of the photocurrent as

$$\begin{aligned} M^\lambda(\epsilon,\omega) = N\frac{4\pi k}{(c\pi)^2\omega^2}\,\Im \sum_{\substack{u\alpha\\ v\beta}} \sum_{LL'} \sum_{L_2L_2'} & U_{L_2}^{u\alpha}(\boldsymbol{k},\tilde{\epsilon}) \mathrm{e}^{\mathrm{i}\boldsymbol{q}\cdot\boldsymbol{S}^{u\alpha}} \\ & \times F_{L_2L}^{u\alpha\lambda(1)}(\epsilon,\omega)\tau_{LL'}^{u\alpha,v\beta}(\boldsymbol{k}_\parallel+\boldsymbol{q}_\parallel;\epsilon) F_{L_2'L'}^{v\beta\lambda(2)}(\epsilon,\omega) \mathrm{e}^{-\mathrm{i}\boldsymbol{q}\cdot\boldsymbol{S}^{v\beta}} U_{L_2'}^{v\beta *}(\boldsymbol{k};\tilde{\epsilon}) \end{aligned} \tag{38}$$

$$I^\lambda(\epsilon,\omega) = N\frac{4\pi k}{(c\pi)^2\omega^2}\,\Im \sum_{u\alpha} \sum_{LL'} U_L^{u\alpha}(\boldsymbol{k},\tilde{\epsilon}) D_{LL'}^{u\alpha,\lambda}(\epsilon,\omega) U_{L'}^{u\alpha *}(\boldsymbol{k};\tilde{\epsilon}) \tag{39}$$

with

$$U_L^{u\alpha}(\boldsymbol{k},\tilde{\epsilon}) = \sum_{L_1} \mathrm{i}^{l_1} Y_{L_1}^*(\hat{\boldsymbol{k}}) \sum_{v\beta} \mathrm{e}^{\mathrm{i}\boldsymbol{k}\cdot\boldsymbol{S}^{v\beta}} \tau_{L_1L}^{v\beta,u\alpha}(\boldsymbol{k}_\parallel;\tilde{\epsilon}). \tag{40}$$

We finish this section with the formula for the layer-resolved Bloch spectral function $A^{u\alpha}(\boldsymbol{k}_\parallel, E)$, which we shall use later for analysing our photoemission results. It reads as

$$A^{u\alpha}(\boldsymbol{k}_\parallel, E) = -\frac{1}{\pi}\int \mathrm{d}^3 r\ \Im G^{u\alpha,u\alpha}(\boldsymbol{r},\boldsymbol{r};\boldsymbol{k}_\parallel, E+\mathrm{i}0^+) \tag{41}$$

and with the 2D lattice Fourier transform of the Green's function:

$$G_{u\alpha,v\beta}(\boldsymbol{r},\boldsymbol{r}';\boldsymbol{k}_\parallel;\epsilon) = \sum_{\boldsymbol{R}_\parallel} \mathrm{e}^{\mathrm{i}\boldsymbol{k}_\parallel\cdot\boldsymbol{R}_\parallel} G(\boldsymbol{r}+\boldsymbol{S}^{u\alpha}+\boldsymbol{R}_\parallel, \boldsymbol{r}'+\boldsymbol{S}^{v\beta};\epsilon) \tag{42}$$

we obtain

$$A^{u\alpha}(\boldsymbol{k}_\parallel, E) = -\frac{1}{\pi}\sum_L \Im\tau_{L,L}^{u\alpha,u\alpha}(\boldsymbol{k}_\parallel; E+\mathrm{i}0^+) \int \mathrm{d}r\ r^2 Z_l^{u\alpha}(r,E)^2. \tag{43}$$

The above is just the angular momentum sum of the L-resolved spectral function:

$$A_L^{u\alpha}(\boldsymbol{k}_\parallel, E) = -\frac{1}{\pi}\,\Im\tau_{L,L}^{u\alpha,u\alpha}(\boldsymbol{k}_\parallel; E + \mathrm{i}0^+)\int \mathrm{d}r\; r^2 Z_l^{u\alpha}(r, E)^2. \tag{44}$$

This spectral function is a very useful quantity, since it gives direct information about the KKR scattering matrix, which is the quantity through which the band structure enters the photocurrent.

3. Application

In this section we demonstrate how the method described above works in practice. As an example, we choose the well studied copper surfaces, and, in particular, we investigate the features of the sp band, seen on the (100) surface, and the surface state on (111). The potentials for the respective calculations were determined self-consistently using the layer KKR method [16, 20, 21, 27]. The potentials for the system, consisting of ten Cu layers and three layers of empty spheres (to represent the vacuum), have been updated self-consistently. In what follows we refer to the surface layer of this system as S and to the subsequent layers below the surface as $S_{-1}, S_{-2}, \ldots$. The empty-sphere layers are denoted by $S_1, S_2, \ldots$. The boundary conditions for both infinite half-spaces are such that the Cu bulk potential has been used for all layers S_{-11} to $S_{-\infty}$ and the empty-sphere potential of the outermost vacuum layer, S_3, has been repeated for S_4 to S_∞. In the calculations these infinite half-spaces have been treated with the decimation technique [28]. Therefore the potentials used for the (100) and (111) surfaces differ from each other. As a demonstration of this, we show in table 1 the work functions evaluated, which were then used in the photoemission calculations.

Table 1. Work functions Φ in eV obtained in this method compared with other theoretical and with experimental values, both taken from references [**?**, 37].

	Present work	Turek	Skriver	Experiment
Cu(100)	5.25	5.21	5.26	4.59
Cu(111)	5.46	5.16	5.30	4.94

Figure 1 shows a series of photoemission spectra for different emission angles. What can be clearly observed here is the d-band feature at binding energies between -2 and -4 eV, and the sp band reaching up to the Fermi level. These results are in good agreement with the experimental spectra and previous calculations [29].

With these spectra to hand, we want to show the relation of the photoemission spectra to the layer-resolved spectral function, defined in equation (41), which is often used to interpret the photoemission data. As opposed to the case for normal-emission experiments, which correspond to $\boldsymbol{k}_\parallel = 0$, for the off-normal emission, one cannot relate each spectrum to one single, well defined $\boldsymbol{k}_\parallel$. The 2D wave vector $\boldsymbol{k}_\parallel$ (see equation (4)) depends on the kinetic energy of the electron and hence on the binding energy. This, of course, can be taken into account, but in the present discussion we calculate the spectral functions for $\boldsymbol{k}_\parallel$ corresponding to the centre of the spectra, i.e. a binding energy of 2 eV. This leads to shifts of the peaks in the outer regions of the plots, but since we only want to compare general features, these shifts are of no practical importance.

Figure 2 shows the spectral functions of the surface layer and the bulk-like S_{-9} layer, corresponding to the spectra shown in figure 1. Note that in the energy range above -2 eV two clear features can be identified in the spectral functions, both stemming from the sp bands. Only one of them can be observed in the photocurrent. This is a clear effect of the matrix elements

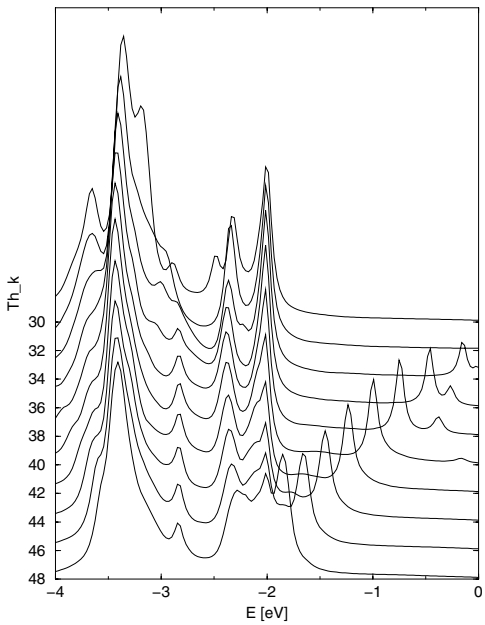

Figure 1. The photocurrent of Cu(100) at 21.2 eV in the ΓXULK plane. The calculations were performed with a hole linewidth of 0.05 eV and an electron linewidth of 1.3 eV. Eleven Cu layers and ten vacuum layers were contributing to the photocurrent, and the KKR matrix was inverted for a system of sixteen Cu and fifteen empty-sphere layers.

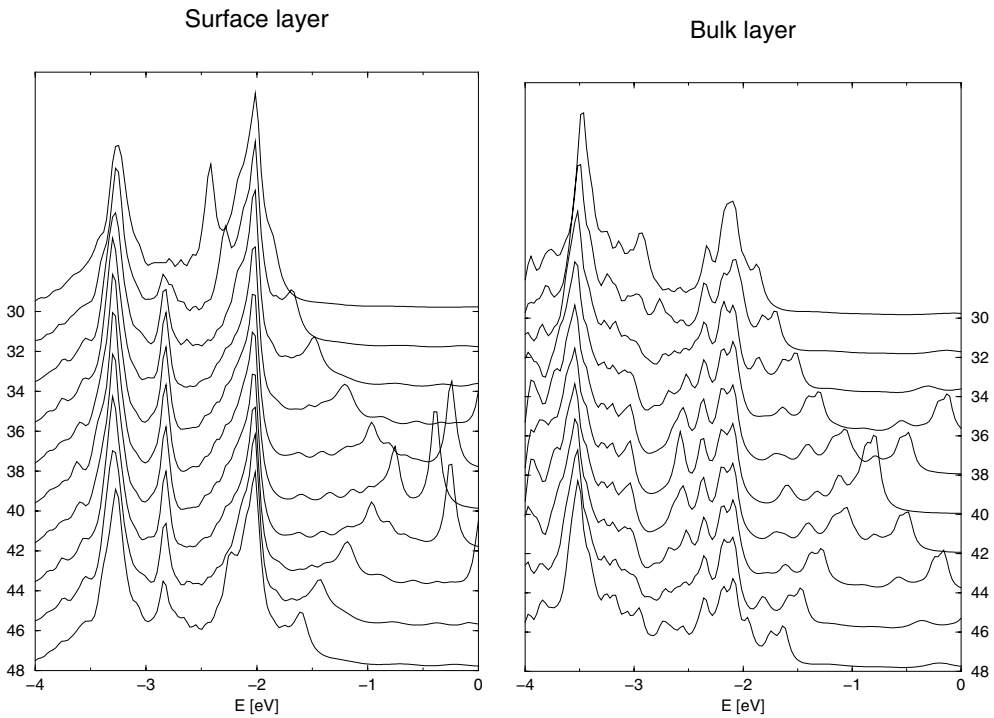

Figure 2. Layer-resolved Bloch spectral functions of the surface and a bulk-like layer. The spectral functions correspond to the emission angles of 30° to 48°.

and the high-energy states, which do not allow excitations from the states corresponding to the second feature in the spectral function. Predicting photoemission spectra on the basis of the

spectral functions alone is therefore not possible. Since it is well known that KS bands might occur at wrong energies, it is not always obvious how to relate the features seen in the spectral function to those observed in the photoemission data. Having calculated the photocurrent, one can relate the peaks in the experimental curve to the calculated ones, and can then use the spectral functions to analyse these features. Here we just want to point out that the small peaks near the Fermi level at the emission angles 34° to 40° can be related to the surface effects. These peaks can be found in the surface layer spectral function, but they are not present in the bulk-like spectral function.

Figure 3 shows the spectral functions corresponding to the 38° spectrum for the top ten layers. This shows that the redistribution of spectral weight is confined to 4–5 layers below the surface. From there on the system behaves basically like the bulk. The extent of 4–5 layers agrees well with the finding that beyond the order of five layers one basically recovers bulk behaviour. The observed differences between the layers deep below the surface can be easily explained as follows: in the bulk the Bloch states describe travelling waves, which give rise to a lattice-periodic spectral function. On introducing a surface, these travelling Bloch waves are reflected at the surface, leading to standing waves, and thus to energy-dependent oscillations in space. The latter can be beautifully observed in the energy range between −2 and −3 eV.

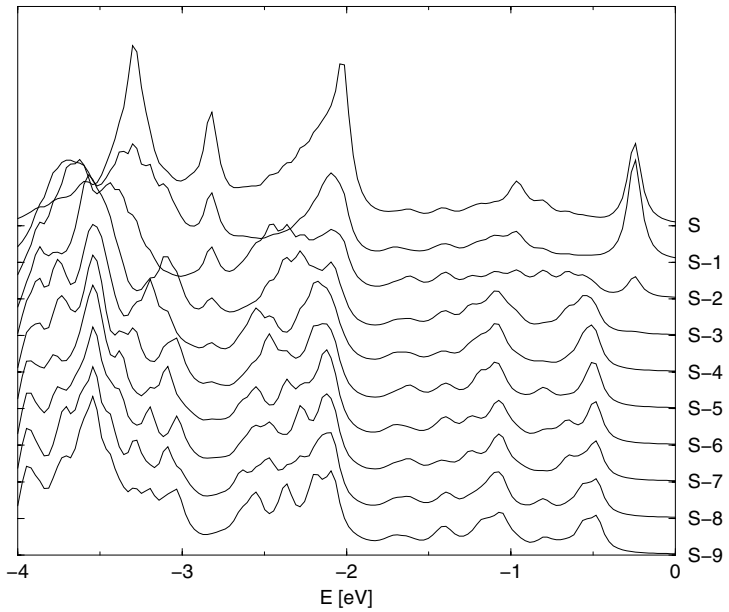

Figure 3. Layer-resolved spectral functions corresponding to an emission angle of 38° for the surface layer and the first nine subsurface layers.

As another example of the interplay between photoemission calculations and the layer-resolved spectral function, we study the surface state on the (111) surface of copper. The experimental [30] and calculated results for the total photocurrent at 21.2 eV photon energy are shown in figures 4 and 5. The surface state is clearly observed at −0.9 eV in the calculations. Since it is only visible with p-polarized light, one can already conclude that the state has Λ_3 symmetry [31]. It is possible to identify the surface state by investigating the layer-resolved spectral function for $\boldsymbol{k}_\parallel = 0$, which corresponds to normal emission.

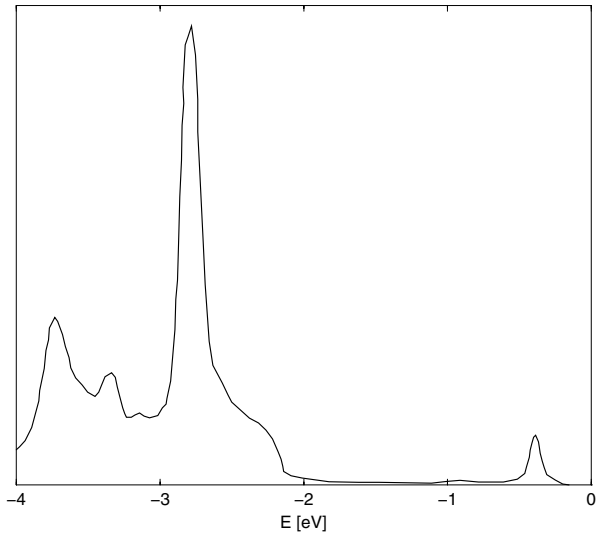

Figure 4. The experimental photocurrent of Cu(111) at 21.2 eV normal emission.

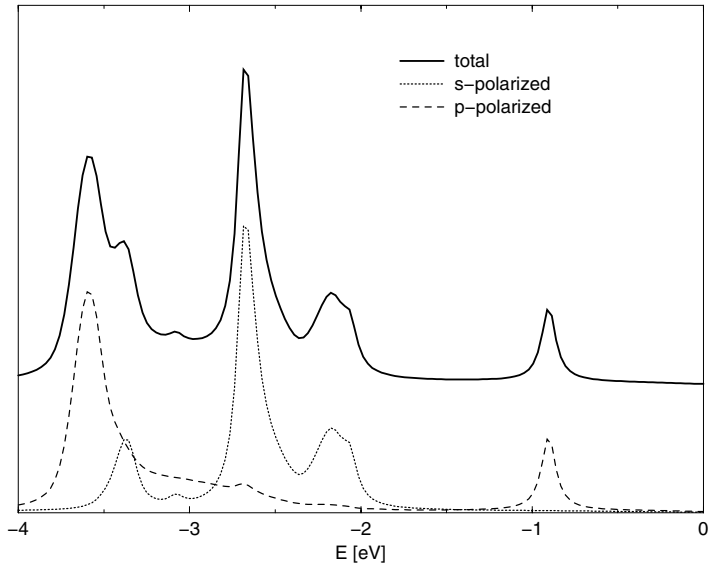

Figure 5. Polarization-resolved photocurrents of Cu(111) at 21.2 eV normal emission.

In figure 6 it can be seen that in the layer-resolved spectral function a peak at -0.9 eV only appears for the layers near the surface, and that it decays quickly when going into the sample. Similarly, it can also be observed that the small peak at about -3 eV originates from a surface state. To gain further insight, one can use the angular-momentum-decomposed spectral function.

In figure 7 we display the angular momentum decomposition of the spectral function at the surface layer. Note that the surface state at -0.9 eV has mainly p character, while the state at -3 eV is derived from a d state. These symmetries are, due to the selection

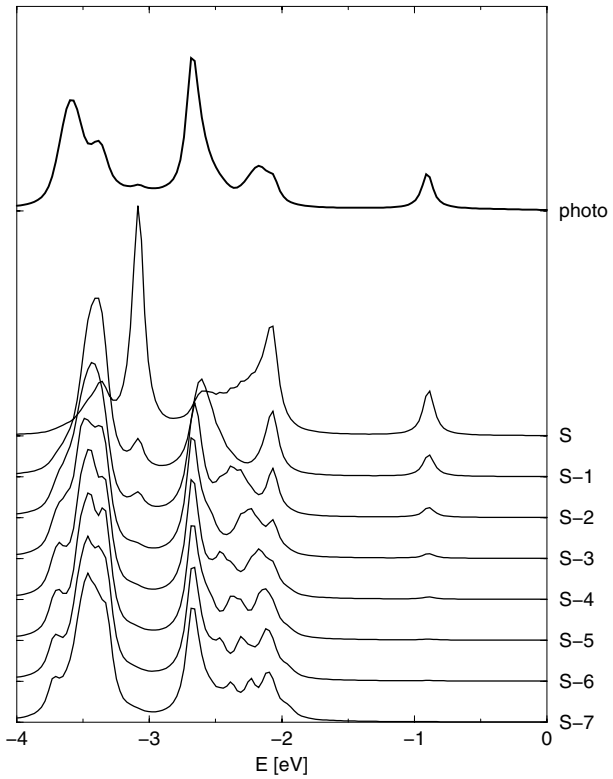

Figure 6. Photocurrents of Cu(111) compared with the layer-resolved Bloch spectral function.

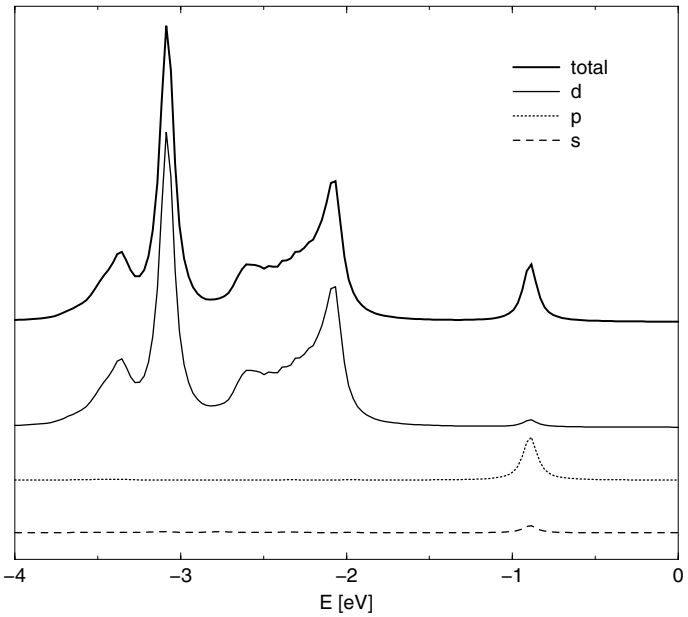

Figure 7. The angular momentum decomposition of the spectral function of the (111) surface layer.

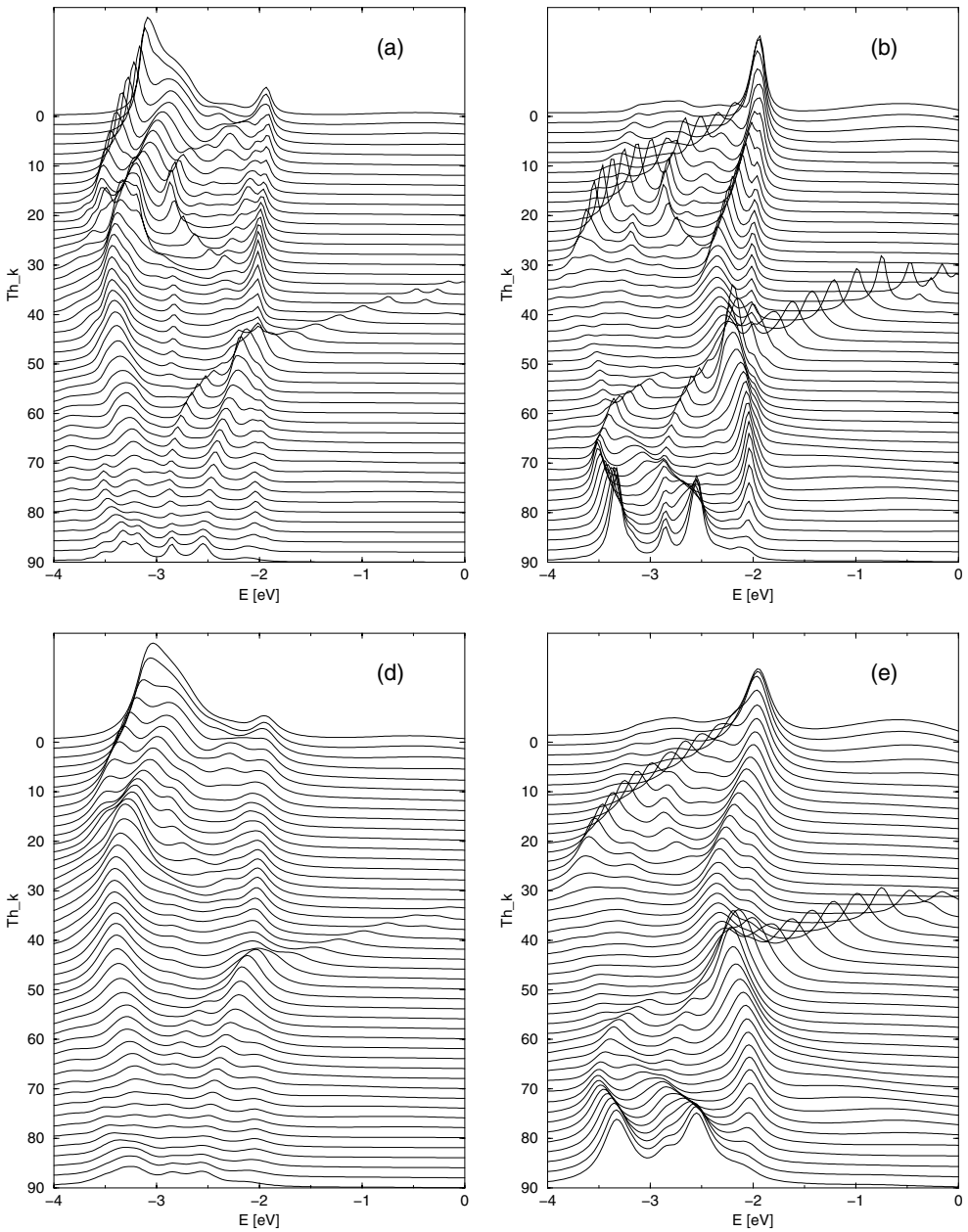

Figure 8. Layer calculations for the (100) surface at 21.2 eV photon energy performed with different imaginary parts of the electron and hole energies, and the single-scatterer approximation. The top row ((a), (b), (c)) shows results for a hole broadening of 0.05 eV, for the bottom row ((d), (e), (f)) 0.13 eV. From left to right the electron broadening is 1.3 eV ((a), (d)) and 4 eV ((b), (e)). The right column ((c), (f)) shows the single-scatterer approximation.

rules, also reflected in the polarization dependence of the photocurrent. The p-like state is of Λ_3 symmetry and shows up only in p-polarized light, while the d-like state is seen in the s-polarization spectrum.

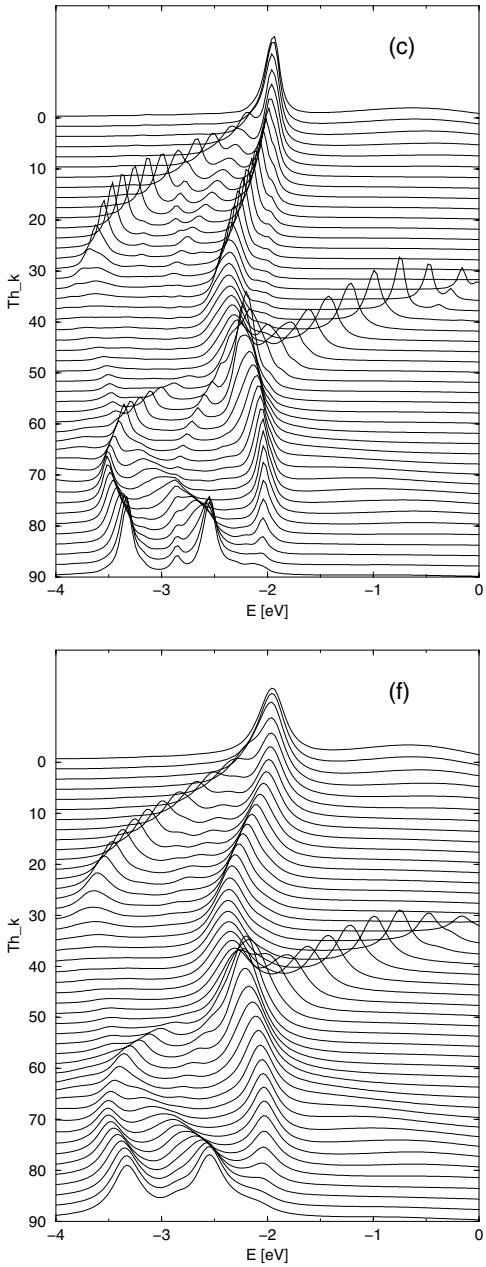

Figure 8. (Continued)

4. Numerical aspects

Using the KS Green's functions for the calculation of the photocurrent, one neglects self-energy effects. The real part of the self-energy gives rise to a shift of the excitation energies. If the aim is to obtain just a qualitative picture of a photoemission spectrum, this real part can in many cases be neglected. The imaginary part leads to a finite lifetime of the excitations and

thus determines the linewidth and also the intensity of the observed peaks. As the initial- or final-state energies move further away from the Fermi level, these lifetime effects become more and more important, and cannot be neglected any longer. In this work we are not presenting a first-principles calculation for these lifetimes (for that, one has to use methods such as the *GW* method [10]), but we simulate them by solving the KKR (Dyson) equation for complex energies, whose imaginary part introduces a finite lifetime. This concept is similar to that of including an optical (imaginary) potential [32], but has the advantage that the numerical difficulties of evaluating the structure constants at real energies are circumvented.

In the following we compare our calculations with different imaginary energies for both holes and electrons. While the imaginary part of the hole energy leads to a plain broadening of the peaks, the effect of the imaginary part of the electron energy is more indirect. It broadens the spectral function of the final state, redistributing the spectral weight, and hence allowing electron excitations into different final states. In figure 8 one can see that whole features are disappearing for larger imaginary parts. This demonstrates vividly the necessity for the inclusion in the calculation of photocurrents of *ab initio* determined self-energies, especially for the high-energy electrons. In the calculations with the optical potentials or complex energies, the choice of the imaginary parts should be made according to the self-energy of the system. Also shown in this figure are the calculations performed with the single-scatterer approximation for the high-energy state. In the single-scatterer approximation the τ-matrix is replaced by the single-site t-matrix, i.e. only the on-site scattering is taken into account [33]. The replacement of the full scattering matrix by a diagonal matrix leads to an enormous speed-up of the code. It can be seen that the results obtained with the single-scatterer approximation and with a final-state broadening of about 4 eV are in very good agreement. The physical reason for this is that the imaginary energy of 4 eV results in such a short mean free path that the electrons are practically not propagating coherently from one site to the next, and therefore only the on-site processes are important. Since the self-energy of electrons is increasing with increasing distance from the Fermi level, the optical potential used for the highly excited states, i.e. large photon energies, is expected to be large enough to allow for the use of the single-scatterer approximation. In addition, due to the finite lifetime, the 'quasi-particles' do not propagate as non-interacting particles; their propagation is limited to a finite range. This gives a justification for calculating the photocurrent in a finite cluster, sufficient in size to encapsulate this mean free path of the quasi-particles, in the real-space version, or a finite slab in the layer code. Localized states, such as d states, are expected to be well described by a finite cluster. In the following we discuss calculations in real space for different system sizes and imaginary energies, and compare them with the layer method results.

This comparison is shown in figure 9. Here several points can be made. First, the sp bands seen in the layer calculation cannot be reproduced with the real-space calculations. Second, the basic features of the d bands can already be reproduced with the 55-atom cluster. The 87-atom cluster shows an improvement in both the d bandwidth and the smoothness of the features, but is still not sufficient to allow one to resolve all details of the spectra. Finally, although in the real-space calculations the imaginary part of 1.4 eV has been used, the results show a closer resemblance to those from the layer calculations, shown in figure 8, with a much larger imaginary part of the electron energies, or even the single-scatterer approximation. By comparing the linewidths seen in figures 8 and 9, one finds also that the hole linewidth in the real-space calculations is larger than that in the layer calculation, although these calculations have been performed with the same imaginary energy for the holes. Furthermore, the effect of the hole broadening in the cluster calculations is much weaker than in the layer calculations. The missing sp bands can be understood as follows: the strongly dispersive sp bands correspond to states which are much more extended than the d states. The cluster size used in the real-space

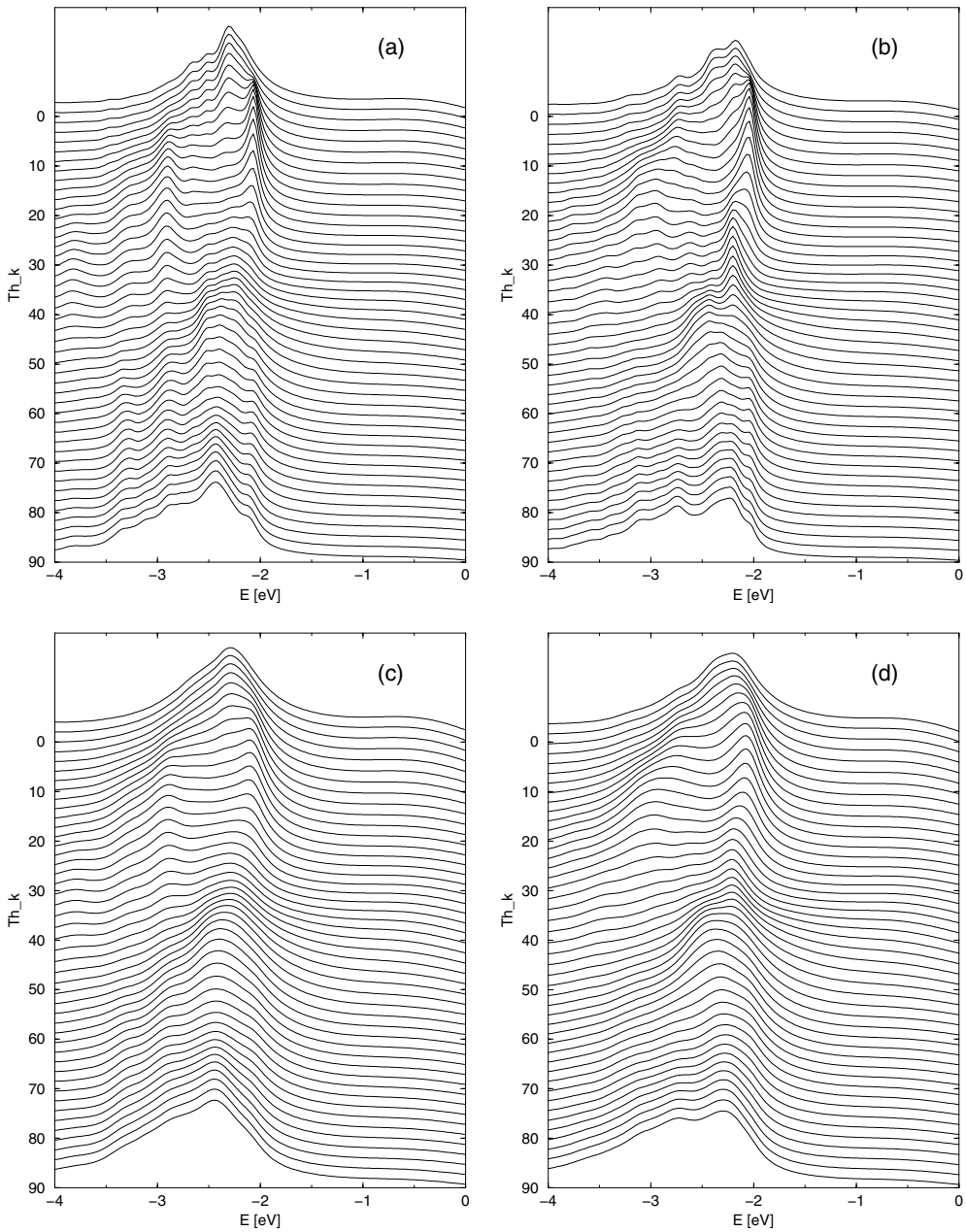

Figure 9. Comparison of real-space and layer calculations. The real-space calculations were performed with 55-atom ((a), (c)) and 87-atom ((b), (d)) clusters for the photocurrent. For the calculation of the τ-matrix two more shells were included, i.e. the clusters contained of 87 and 141 atoms respectively. The calculations (a), (b) used an imaginary part of 0.05 eV for the lower state, while for (c), (d) 0.13 eV was used. The real-space calculations were performed with a 1.3 eV broadening for the high state.

calculations is too small to allow for the propagation of sp-like electrons. It should be kept in mind that in the layer method, even if the system is represented by a finite slab, the infinite

extent in the xy-plane is treated quasi-exactly (Kambe's method [34–36] of calculating 2D lattice sums is used). The d states, on the other hand, which have a smaller bandwidth and hence are more localized, are more readily accessible using real-space cluster calculations. From the last point one can conclude that in the present calculations the broadening of the electrons and holes is dominated by the mean free path, introduced by the cluster size and not by the mean free path due to the imaginary energies. A comparison to the layer calculations with large imaginary energies of the electrons shows that the mean free path introduced by the finite cluster corresponds to a broadening of the order of several eV.

The influence of the system size on the layer calculations can be seen in figure 10. The two calculations use the same potentials and the same broadenings, but differ as regards the slab size used in the photoemission calculation. For the results shown in the left-hand panel a slab of 16 Cu and 15 empty sphere layers was used in the calculation of the scattering matrix, while 11 Cu and 10 empty-sphere layers were taken into account for the photocurrent. This system size was also used for all other layer calculations in this paper. The right-hand panel shows the results of the calculations with 31 Cu and 30 empty-sphere layers for the τ-matrix, and 26 and 25 layers for the photocurrent. It is clear that the sp features are more pronounced in the larger slab. This was to be expected on the grounds of the above explanation of the missing sp features in the cluster calculation.

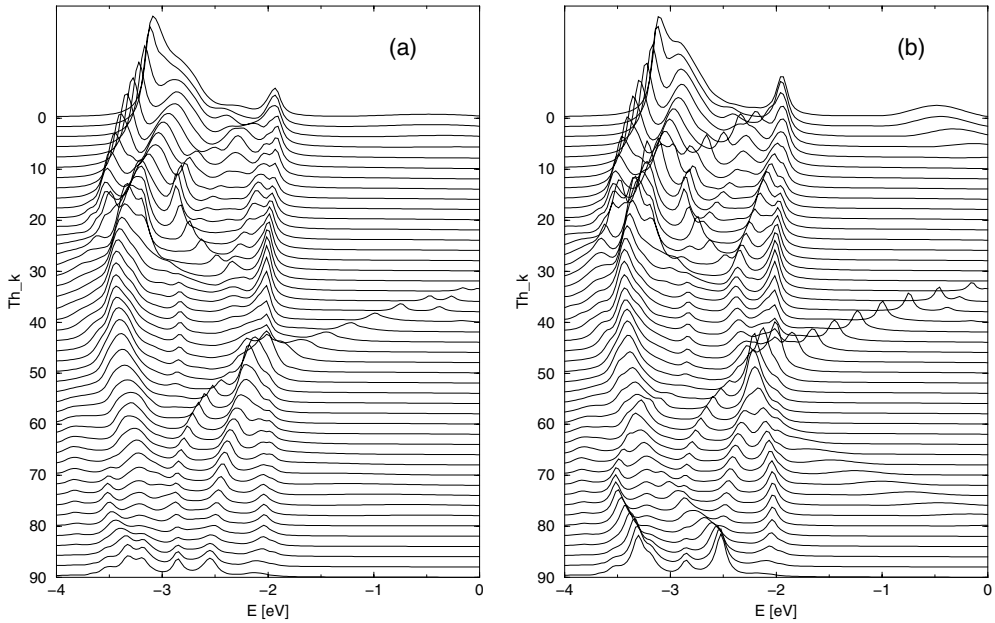

Figure 10. Comparison of layer calculations with different slab sizes. The number of layers for the photocurrent (the τ-matrix) are, in (a): 11 (16) Cu layers and 10 (15) empty-sphere layers; and in (b): 26 (31) Cu layers and 25 (30) empty-sphere layers.

In many previous photoemission calculations the surfaces were treated by using the bulk potentials with a model description of the vacuum barrier potential. In the present method, the potentials can be taken directly from the self-consistent calculation for the specific geometry, i.e. the potentials of the surface layers and the vacuum layers on top of the surface are calculated on the same footing as the bulk potentials, which serve as the correct boundary conditions. In figure 11 we compare results obtained with the self-consistently calculated potentials to the

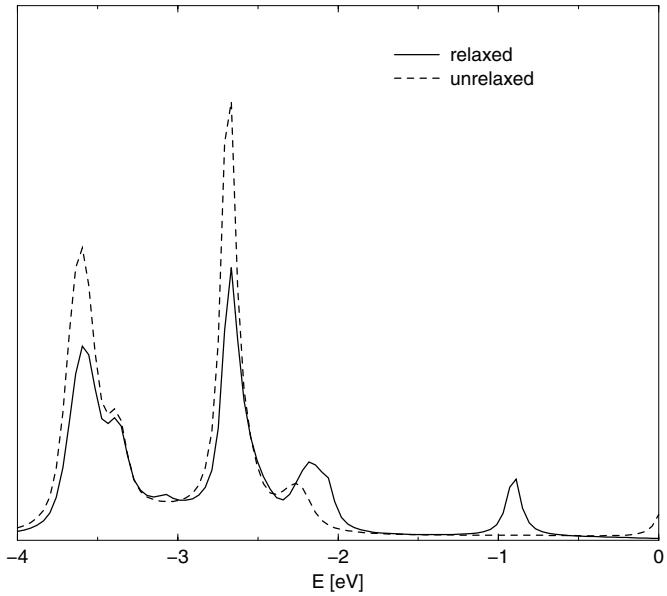

Figure 11. Comparison of relaxed and unrelaxed potentials (see the text for details).

results calculated with the bulk potentials only. Here for all Cu layers the bulk potential was used, while for all vacuum layers (S_1 to S_∞) the 'vacuum–bulk' potential (S_3) was used. As should have been expected, we find good agreement for the bulk-like features, while the surface states are strongly affected by the slight changes of the potentials and the resulting redistribution of charge. These results are in perfect agreement with those given by Turek *et al* [37]. Since the position of the surface state is so sensitive to the details of the surface potential, the shift of the calculated surface state with respect to the experimentally observed surface state can be explained by the deviation of the calculated work function from the experimental value, given in table 1.

For the calculation of the scattering matrices, different methods can be applied. In figure 12 we compare three different methods, applied to the low-energy states. Firstly, the structure constants can be calculated for a real-space cluster. The screening transformation, introduced by Andersen [38, 39], can be applied to make the structure constants short ranged. Therefore, the reference system is replaced by a system with a repulsive potential [17], which forbids free-electron propagation below the height of the repulsive potential, and hence leads to short-ranged structure constants. In the case of the 2D lattice periodicity, the Fourier transform of the screened structure constants can easily be evaluated [27]. Secondly, the structure constants can be evaluated by the Kambe method [34–36], making use of the 2D lattice symmetry. Finally, the two methods can be combined, giving rise to the screened Kambe structure constants [40]. In all these cases, however, the same layer geometry was used. The differences between the curves are very small and demonstrate that all methods have about the same accuracy, proving that all the different structure constants have been converged.

5. Conclusions

We have presented an implementation of the real-space scattering-matrix method for calculating photoemission spectra for arbitrary geometries, such as surfaces and impurities.

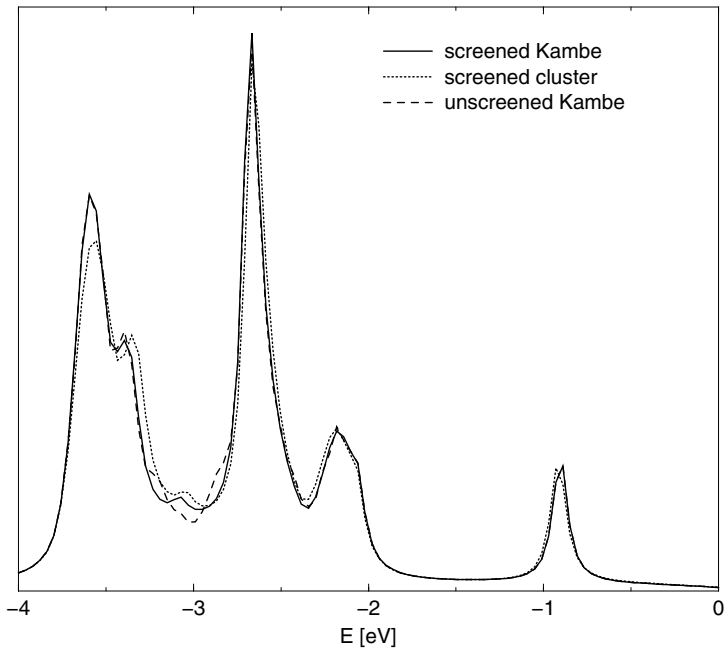

Figure 12. Comparison of different methods for calculating the low-energy scattering matrix.

The main feature of this approach is its flexibility. The formalism, developed in real space, is easily adapted to 2D lattice symmetry. Several methods for calculating the required scattering matrices are available and can be used. For the initial states, the screened KKR implementation can be employed, which together with the decimation technique eliminates finite-size effects for the hole states and allows for fast computations of the scattering matrix. Another strong point of this method is that the self-consistent calculation and the calculations of the spectral functions and the photocurrent are based on the same method and are performed with the same code.

We demonstrated the power of the method for interpreting experimental spectra, by investigating the spectral functions calculated within the same method. This combination provides insight into the nature of the photoemission peaks. It was shown that a comparison of the experimental results with calculations of the Bloch spectral function alone might not always be sufficient. This combination of spectral functions and photocurrent calculations was applied to the photoemission spectra of the copper (100) and (111) surfaces.

Comparisons of real-space calculations with the layer calculations showed that the real-space method, which provides much more flexibility than the layer method, yields good results for localized states, such as d states, which are well described by a finite-cluster calculation. This was illustrated by calculations performed with the layer method, where the mean free path of the electrons and holes was limited by the introduction of an imaginary part in the energies. With increasing imaginary energies the results showed closer agreement with the real-space results. Further improvement on the real-space method can be achieved by implementing the screening transformation also in the real-space code. This would on the one hand make the structure constants short ranged, and hence improve the cluster approximation, and would also, due to the resulting sparsity of the scattering matrix, allow bigger clusters to be investigated.

Acknowledgments

We would like to thank R Blake, P Dederichs, J Henk, P Strange, L Szunyogh, P Weinberger, H Winter, and M Woods for valuable discussions. Part of the work was supported by the European Union through the Training and Mobility of Researchers network (TMR) on magnetic multilayers.

References

[1] Feng D L, Lu D H, Shen K M, Kim C, Eisaki H, Damascelli A, Yoshizaki R, Shimoyama J, Kishio K, Gu G D, Oh S, Andrus A, O'Donnell J, Eckstein J N and Shen Z X 2000 *Science* **289** 277
[2] Kaminski A, Mesot J, Fretwell H, Campuzano J C, Norman M R, Randeria M, Ding H, Sato T, Takahashi T, Mochiku T, Kadowaki K and Hoechst H 2000 *Phys. Rev. Lett.* **84** 1788
[3] Himpsel F J 1999 *J. Phys.: Condens. Matter* **11** 9483
[4] Dallmeyer A, Carbone C, Eberhardt W, Pampuck C, Gustav W, Gambarella P and Kern K 2000 *Phys. Rev.* B **61** R5133
[5] Dowben P A, McIlroy D N and Li Dongqi 1997 *Handbook on the Physics and Chemistry of Rare Earths* vol 24, ed K A Gschneidner Jr and L Eyring (Amsterdam: North-Holland) p 1
[6] Arko A J, Riseborough P S, Andrews A B, Joyce J J, Tahvildar-Zadeh A N and Jarrell M 1999 Photoelectron spectroscopy in heavy fermion systems: emphasis on single crystals *Handbook on the Physics and Chemistry of Rare Earths* vol 26, ed K A Gschneidner Jr and L Eyring (Amsterdam: North-Holland) p 172
[7] Hohenberg P and Kohn W 1964 *Phys. Rev.* **136** B864
[8] Kohn W and Sham L J 1965 *Phys. Rev.* **140** A1133
[9] Dreizler R M and Gross E K U 1990 *Density Functional Theory* (Berlin: Springer)
[10] Hedin L and Lundqvist S 1969 *Solid State Physics* vol 23, ed H Ehrenreich, F Seitz and D Turnbull (New York: Academic)
[11] Feibelman P J and Eastman D E 1974 *Phys. Rev.* B **10** 4932
[12] Pendry J B 1976 *Surf. Sci.* **57** 679
[13] Györffy B L and Stott M J 1973 *Band Structure Spectroscopy of Metals and Alloys (NATO)* ed D J Fabian and L M Watson (New York: Academic) p 385
[14] Korringa J 1947 *Physica* **13** 342
[15] Kohn W and Rostoker N 1954 *Phys. Rev.* **94** 1111
[16] Szunyogh L, Újfalussy B, Weinberger P and Kollár J 1994 *Phys. Rev.* B **49** 2721
[17] Zeller R, Dederichs P H, Újfalussy B, Szunyogh L and Weinberger P 1995 *Phys. Rev.* B **52** 8807
[18] Moghadam N Y, Stocks G M, Újfalussy B, Shelton W A, Gonis A and Faulkner J S 1999 *J. Phys.: Condens. Matter* **11** 5505
[19] Petit L, Beiden S V, Temmerman W M, Szotek Z, Stocks G M and Gehring G A 2000 *J. Phys.: Condens. Matter* **12** 8439
[20] Ernst A, Lüders M, Temmerman W M, Szotek Z and van der Laan G 2000 *J. Phys.: Condens. Matter* **12** 5599
[21] Ernst A, van der Laan G, Temmerman W M, Dhesi S S and Szotek Z 2000 *Phys. Rev.* B **62** 9543
[22] Durham P J 1984 *The Electronic Structure of Complex Systems (NATO ASI Series B: Physics, vol 113)* ed P Phariseau and W M Temmerman (New York: Plenum) p 709
[23] Durham P J 1981 *J. Phys. F: Met. Phys.* **11** 2475
[24] Ernst A, Temmerman W M, Szotek Z, Woods M and Durham P J 1998 *Phil. Mag.* B **78** 503
[25] Caroli C, Lederer-Rozenblatt D, Roulet B and Saint-James D 1973 *Phys. Rev.* B **8** 4552
[26] Gonis A 1992 *Green Functions for Ordered and Disordered Systems* (Amsterdam: North-Holland)
[27] Wildberger K, Zeller R and Dederichs P H 1997 *Phys. Rev.* B **55** 10 074
[28] Godfrin E M 1991 *J. Phys.: Condens. Matter* **3** 7843
[29] Durham P J and Kar N 1981 *Surf. Sci.* **111** L648
[30] Fluchtmann M, Bei der Kellen S, Braun J and Borstel G 1998 *Surf. Sci.* **402–404** 663
[31] Hüfner S 1995 *Photoelectron Spectroscopy (Springer Series in Solid-State Science vol 82)* (Berlin: Springer)
[32] Pendry J B 1974 *Low Energy Electron Diffraction* (New York: Academic)
[33] Winter H, Durham P J and Stocks G M 1984 *J. Phys. F: Met. Phys.* **14** 1047
[34] Kambe K 1967 *Z. Naturf.* a **22** 322
[35] Kambe K 1967 *Z. Naturf.* a **22** 422
[36] Kambe K 1968 *Z. Naturf.* a **23** 322

[37] Turek I, Drchal V, Kurdnovský J, Sob M and Weinberger P 1997 *Electronic Structure of Disordered Alloys, Surfaces and Interfaces* (Dordrecht: Kluwer Academic)
[38] Andersen O K and Jepsen O 1984 *Phys. Rev. Lett.* **53** 2571
[39] Andersen O K, Postnikov A V and Savrasov S Yu 1992 *Application of Multiple Scattering Theory to Materials Science (MRS Symp. Proc. No 253)* ed W H Butler, P H Dederichs, A Gonis and R L Weaver (Pittsburgh, PA: Materials Research Society)
[40] Uiberacker C, Szunyogh L, Újfalussy B, Weinberger P, Ernst A and Dederichs P H 1998 *Phil. Mag.* B **78** 423